ACS Energy LETTERS

This is an open access article published under a Creative Commons Attribution (CC-BY) License, which permits unrestricted use, distribution and reproduction in any medium, provided the author and source are cited.

ACS AUTHORCHOICE

http://pubs.acs.org/journal/aelccp

Control over Crystal Size in Vapor Deposited Metal-Halide Perovskite Films

Kilian B. Lohmann, Jay B. Patel, Mathias Uller Rothmann, Chelsea Q. Xia, Robert D. J. Oliver, Laura M. Herz, Henry J. Snaith, and Michael B. Johnston*

Cite This: *ACS Energy Lett.* 2020, 5, 710−717

Read Online

ACCESS | Metrics & More | Article Recommendations | Supporting Information

ABSTRACT: **Understanding and controlling grain growth in metal halide perovskite polycrystalline thin films is an important step in improving the performance of perovskite solar cells. We demonstrate accurate control of crystallite size in $CH_3NH_3PbI_3$ thin films by regulating substrate temperature during vacuum co-deposition of inorganic (PbI_2) and organic (CH_3NH_3I) precursors. Films co-deposited onto a cold (−2 °C) substrate exhibited large, micrometer-sized crystal grains, while films that formed at room temperature (23 °C) only produced grains of 100 nm extent. We isolated the effects of substrate temperature on crystal growth by developing a new method to control sublimation of the organic precursor, and $CH_3NH_3PbI_3$ solar cells deposited in this way yielded a power conversion efficiency of up to 18.2%. Furthermore, we found substrate temperature directly affects the adsorption rate of CH_3NH_3I, thus impacting crystal formation and hence solar cell device performance via changes to the conversion rate of PbI_2 to $CH_3NH_3PbI_3$ and stoichiometry. These findings offer new routes to developing efficient solar cells through reproducible control of crystal morphology and composition.**

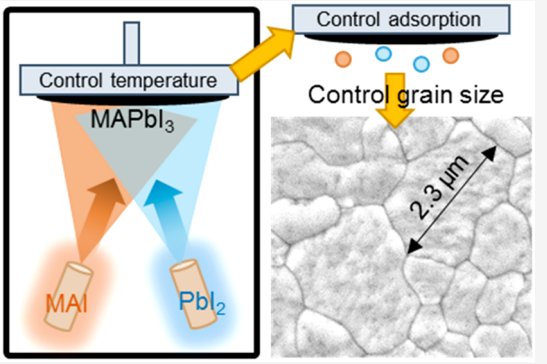

Metal-halide perovskites (MHPs) are a novel class of semiconductors first employed in a solar cell in 2009.[1] These semiconductors have the potential to revolutionize the field of photovoltaics due to their versatility and ease of fabrication.[2] While silicon-based solar cells are currently dominating the market, MHP-based cells have experienced unprecedented growth in solar to electrical power conversion efficiencies (PCEs) in the past decade, recently reaching a certified efficiency of 25.2%.[3] This PCE is already higher than those of polycrystalline-silicon based cells and close to the 26.7% certified PCE of single crystal silicon photovoltaics (PV), and MHPs come with the significant advantage of band gap tunability.[4−8] This makes them ideal candidates for tandem solar cells, be it in all-perovskite configurations[9,10] or with established silicon technologies.[11] With certified efficiencies of 28.0% recently demonstrated for monolithic perovskite-on-silicon tandems,[3,12] these cells are on the brink of revolutionizing the PV market by reducing the overall costs per unit of energy produced.

Because of its low infrastructure cost, the most common fabrication method for MHP cells has been lab-scale solution processing with deposition through spin-coating. Physical vapor deposition, a method in which precursors are sublimed onto substrates under high vacuum, offers multiple advantages, including accurate thickness control and low substrate temperatures as well as avoiding the toxic solvents typically used in solution processing.[13] In light of recent advances in tandem cells, vapor deposition also provides a highly controllable thin-film deposition method for processing multiple layers without damaging the underlying layers.[14] Furthermore, vapor deposition offers an easy route to commercial upscaling of MHP cells, with it already being used in existing technologies such as organic light-emitting diodes (OLEDs) and other thin-film PV technologies.[13] The highest efficiency obtained for fully vacuum processed MHP devices is 20.3% to date,[15] using the prototypical MHP $CH_3NH_3PbI_3$ ($MAPbI_3$). This compound readily forms with a perovskite crystal structure in the presence of just two precursor vapors, namely, the organic methylammonium idoide (CH_3NH_3I, MAI) and inorganic PbI_2. More recently, significant progress has been made in developing physical vapor deposition methods for the more complex alloys that will be ideal for optimized tandem devices.[16−19]

Received: January 26, 2020
Accepted: February 4, 2020
Published: February 4, 2020

Downloaded via UNIV OF OXFORD on February 17, 2020 at 15:42:51 (UTC).
See https://pubs.acs.org/sharingguidelines for options on how to legitimately share published articles.

© XXXX American Chemical Society

https://dx.doi.org/10.1021/acsenergylett.0c00183
ACS Energy Lett. 2020, 5, 710−717

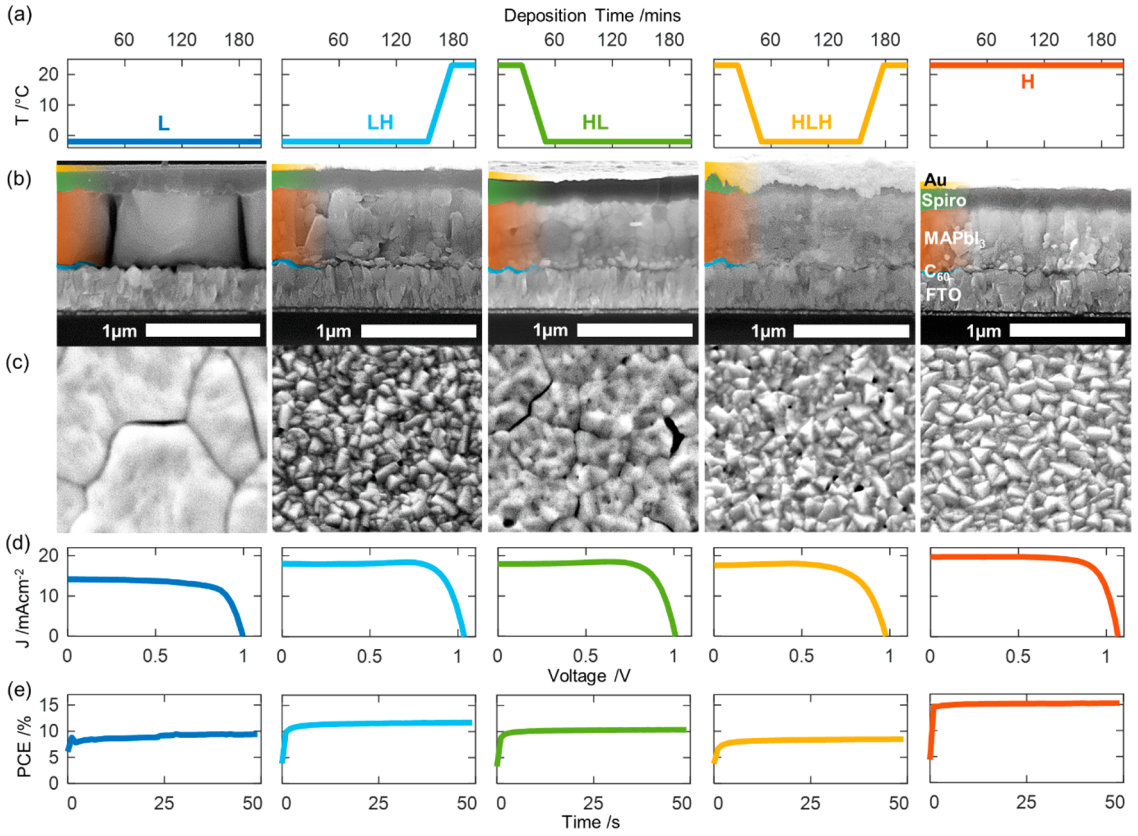

Figure 1. Scanning electron microscopy (SEM) images of co-evaporated $CH_3NH_3PbI_3$ ($MAPbI_3$) devices deposited at 5 different substrate temperature conditions over 204 min, as graphically depicted in (a). (b) Cross-sectional images of full devices with the following structure: Fluorene-doped tin oxide (FTO)/C_{60} (blue)/$MAPbI_3$ (orange)/Spiro-OMeTAD (green)/Au (yellow). (c) Top-down images of the same devices after removal of the gold and spiro layer. The scale bar represents 1 μm for both top-down and cross-sectional images. (d, e) J–V curves and steady-state PCE for the devices on which SEM was done, measured under simulated AM1.5 100 mW cm^{-2} irradiance. Further details of device fabrication, scan parameters, and additional images can be found in the Supporting Information.

Despite this remarkable progress, the perovskite vacuum deposition process and growth mechanism is currently poorly understood, particularly owing to the volatile and nondirectional nature of the organic precursor vapor as it leaves the crucible.[13] Indeed, Borchert et al. recently demonstrated that the adsorption rate of MAI is highly sensitive to impurities present in the material, with purified precursors not depositing on some surfaces.[20] This issue presents a significant hurdle for co-deposition, the deposition process where all precursors are sublimed simultaneously,[15,16,21,22] as the sublimation rate of the precursors is typically controlled by tracking the material deposited on quartz microbalances placed near the crucibles. Several methods have been devised to account for the irreproducibility of MAI sublimation. These include multilayer sequential deposition of the precursors,[23] a method where the precursors are sublimed one after the other rather than together, as well as controlling precursor sublimation rate by monitoring the chamber pressure in sequential[24] and co-evaporation routes.[20,25,26] However, sequential methods are less suited to automation due to requiring a post-deposition annealing step, while the co-evaporation pressure control routes have so far yielded poorer performance.

In parallel, a fundamental, unresolved question in the field of MHP photovoltaics is the mechanism by which crystal grain boundaries in MHP films affect solar cell performance. There are a range of studies reporting the benefits of large (micrometer size) grains in solution processed MHP devices,[27−30] and these reports are consistent with grain boundaries having a negative effect on device performance through a high density of charge trapping and recombination centers. In contrast, other studies have found grain boundaries in MHP solar cells to have a benign, if not beneficial, nature,[31−33] with notably Adhyaksa et al. finding both detrimental and beneficial grain boundaries within the same film.[34] Moreover, vacuum processed devices have managed to reach efficiencies up to 20.3% with very small crystal grains, having an approximate lateral extent of just 100 nm;[15,21,35] this indicates more benign grain boundaries in these evaporated MHP films. Understanding the mechanism that causes grain boundaries to be detrimental or benign is therefore a crucial step in improving and reproducing the performance of MHP solar cells.

To elucidate these issues, we devised a method to control the grain size of vacuum deposited films by tuning and varying the temperature of the substrate on which the films form. There are numerous reports of the effects of substrate temperature on solution processed devices;[28,36−39] however, for vacuum deposited films, an additional complication arises. Specifically, for vacuum co-deposition, the substrate temperature affects not only crystal growth dynamics, but also the sticking coefficient and hence adsorption rate of the organic precursor vapor onto the film.[20,40] Thus, even if the sublimation flux of an organic precursor can be controlled, the flux actually involved in forming the MHP film will change

https://dx.doi.org/10.1021/acsenergylett.0c00183
ACS Energy Lett. 2020, 5, 710−717

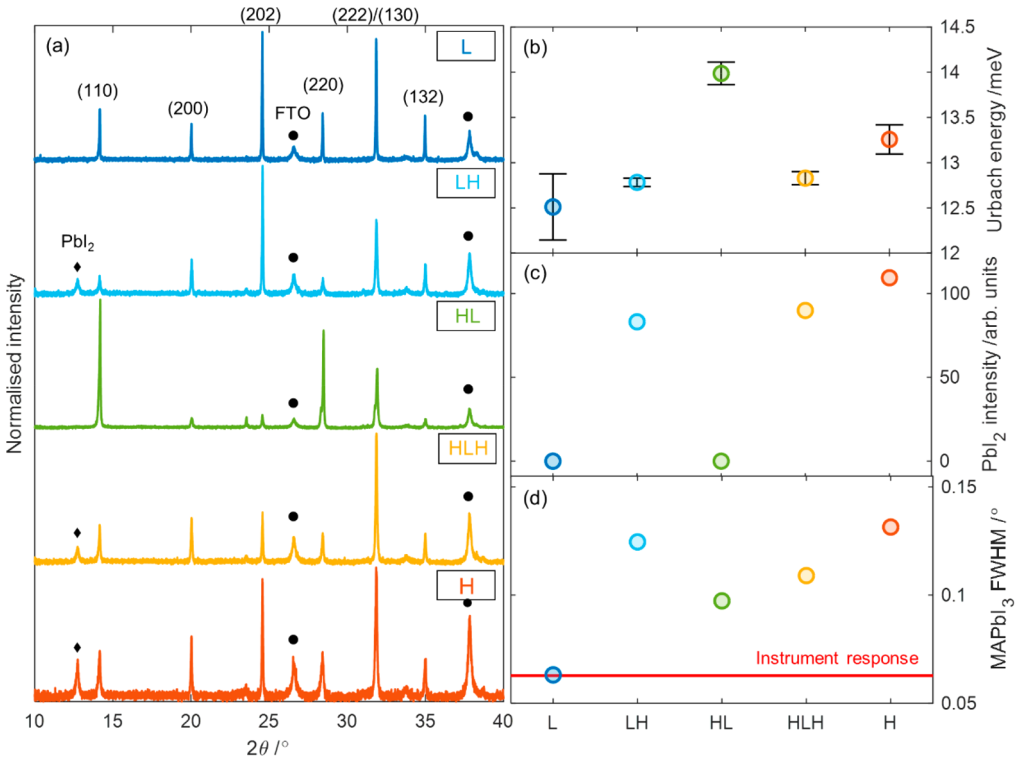

Figure 2. (a) XRD spectra of devices made via the five deposition conditions, after removal of background, normalized to the highest peak, and corrected for angular tilt by using the FTO (110) peak at 26.5°. The black diamonds represent the PbI_2 (001) peak at 12.7°, the black circles show the position of FTO peaks, while the rest of the peaks are from tetragonal $MAPbI_3$, as denoted by the indices. (b) Mean Urbach energy measurements for the corresponding devices. (c) Unnormalized peak intensity of the PbI_2 (001) peak at 12.7°, as calculated from the pseudo-Voigt fit. (d) Full width at half-maximum (fwhm) of the $MAPbI_3$ (222)/(130) peak at 31.9°, as calculated from the pseudo-Voigt fit. The red line represents the instrument broadening, calculated from a Si reference. XRD measurements were taken with a Cu Kα X-ray source; additional information on the equipment and fitting methods can be found in the Supporting Information.

as the film's temperature varies. To investigate all effects related to substrate temperature and deal with the issue of poor process control, we have developed a vacuum co-deposition method by which the flux of organic precursor *adsorbing* to a MHP film is regulated.

Conventional vacuum co-deposition requires a furnace for each precursor material, with a separate quartz microbalance placed just above each furnace to measure the flux sublimed of only that precursor. This allows for the flux sublimed from each furnace to be controlled independently, by adjusting the furnace temperature based on the signal from the respective quartz microbalance. In the case of co-deposition of MAI and PbI_2, this method works well for the inorganic precursor but, as discussed above, is problematic for controlling the flux of the organic precursor, especially if the temperature of the deposition substrate changes.

Our method uses a different configuration, in which the flux of the inorganic precursor (PbI_2) is kept constant in the way described above, but the temperature of the furnace containing the organic precursor (MAI) is set based on a quartz microbalance located near the substrate (the rate measured by this sensor is henceforth denoted as "substrate rate"). Because PbI_2 is deposited on the substrate sensor as well, MAI was found to adhere much more consistently. Furthermore, as the rate of PbI_2 deposition is measured separately by the quartz microbalance situated near its crucible, the flux of MAI can be calculated by comparing the "substrate" rate to the measured PbI_2 rate. Using this method we obtained large, micrometer-sized grains at low temperatures (−2 °C) and smaller, 100 nm grains at room temperature.

$CH_3NH_3PbI_3$ ($MAPbI_3$) solar cells were prepared through vacuum co-evaporation using the substrate rate control method outlined above. During the deposition, the temperature of fluorinated tin oxide (FTO) coated glass substrates was tuned according to five regimes, as represented graphically in Figure 1a. To demonstrate fully the effect of substrate temperature, the substrate rate was always measured on a quartz crystal monitor held at room temperature. In this way, the overall flux of vapor incident on the substrates was the same for all substrate temperatures, thereby isolating resulting differences in morphology to effects of substrate temperature on vapor adsorption and growth mechanisms. Following co-deposition, the samples were not annealed, as this was found to have a negative effect on performance (see Figure S1). The device architecture followed an n−i−p structure on FTO coated glass using undoped C_{60} as the electron transport layer (ETL) and doped 2,2′,7,7′-tetrakis[*N*,*N*-di(4-methoxyphenyl)amino]-9,9′-spirobifluorene (Spiro-OMeTAD) as the hole transport layer (HTL). Additional information on device fabrication and experimental setup is available in the Supporting Information.

Figure 1b and c show an initial inspection of the films with scanning electron microscopy (SEM) and reveal a strong dependence of the film morphology on substrate temperature: large, micrometer-sized grains are formed at low temperatures (−2 °C) (sample L), while warmer conditions (23 °C) led to the appearance of smaller grains throughout the film (sample H). The current−voltage (J−V) and steady-state PCE curves

https://dx.doi.org/10.1021/acsenergylett.0c00183
ACS Energy Lett. 2020, 5, 710−717

(Figure 1d and e) were measured from these devices under AM1.5 simulated sunlight (1 kW/m^2) and show the opposite to what one would expect, with the large grains leading to the worst performance owing to a notably lower current density. To separate the effects of temperature on bulk material and interfaces, we grew three more films of $MAPbI_3$ at low temperature (L), but with thin layers of $MAPbI_3$ deposited at room temperature (H) at either the top (LH), bottom (HL), or both (HLH) interfaces with the charge transport layers (CTL), resulting in partially improved current. The effect of the temperature gradient is well demonstrated in the SEM image of the high-end to low-end temperature sample HL, which shows small grains at the interface, but larger grains throughout the rest of the film. Evidence from the other two conditions is less conclusive, but the low-end to high-end (LH) sample does show enlarged grains throughout the cross section while still having a surface morphology similar to HLH and H, which also finished their growth at room temperature. We further investigated the nature of the gaps between the grains seen in the cross section of L and found them to originate from electron beam damage during SEM imaging (Figure S2). In addition, an enlarged version of the SEM images of Figure 1 (Figure S3) as well as lower magnification images with a larger field of view are also available in the Supporting Information (Figures S4 and S5) for enhanced clarity.

It is worth noting the striking resemblance between the morphology of our low temperature films (L) (Figure 1b and c) and those obtained through sequential deposition by Hsiao et al.,[24] who obtained large grains by fine-tuning the stoichiometry of the films. This similarity in appearance is particularly surprising given Hsiao et al. had a very different nucleation process, since their perovskite formed from a predeposited layer of PbI_2 exposed to MAI vapor. This suggests that film stoichiometry could play a significant role in grain growth, as will be discussed later.

We also investigated the effects of substrate material by growing films on bare FTO, FTO/PolyTPD, indium tin oxide (ITO)/C_{60}, and crystalline silicon and found the nature of the substrate to play an important role in the growth of crystallites: micrometer-sized grains were only observed on FTO/C_{60} (Figures S6 and S7). This finding has important consequences for the choice of transport layers for vacuum co-evaporated perovskite films, since it implies that grain growth is dependent on the substrate, most likely owing to differences in crystal nucleation.

The other striking difference between the layers grown at different temperatures is the thickness of the films. Indeed, sample H is noticeably thinner than the rest of the films, indicating that less material is deposited at higher substrate temperatures. Because the flux of vapor present near the substrate is controlled to be the same for all conditions, substrate temperature has a direct effect on the adsorption rate of the precursor vapor. To investigate whether this leads to any stoichiometric changes and elucidate the poor performance of large grains, the films were further characterized with crystallographic measurements.

The X-ray diffraction (XRD) spectra of the devices after removal of the gold electrode (Figure 2a) show no significant peak shifts between the different growth regimes, but films that finish at room temperature (LH, HLH, H) are characterized by the presence of a (001) PbI_2 peak at 12.7° (Figure 2c). The presence of this peak indicates unconverted, crystalline PbI_2 in the films and points to a stoichiometric imbalance. Along with the evidence from SEM cross sections indicating lower deposition rates at higher temperatures, this suggests that adsorption of MAI vapor is more affected by substrate temperature than PbI_2 and that the stoichiometry hence changes with substrate temperature. For the amount of MAI vapor introduced into the chamber for these devices, full conversion is only achieved at low temperatures. Interestingly, HL, whose growth started at room temperature, does not have crystalline excess PbI_2. This is likely the result of excess PbI_2 from the initial room temperature deposition phase subsequently being converted to $MAPbI_3$ by the additional MAI adsorbed during the low temperature deposition phase.

The full width at half-maximum (fwhm) of XRD peaks give a measure of crystal quality through the Scherrer equation, which shows the former to be inversely proportional to the crystallite size in the direction perpendicular to the substrate.[41] This broadening of the XRD peaks originates from the finite number of lattice planes that coherently scatter the X-rays. The fwhm values were calculated by fitting a pseudo-Voigt distribution to the relevant peaks, while the instrument response was calculated from a reference measurement of a single-crystal silicon wafer. A detailed description of the fitting procedures can be found in the Supporting Information. Figure 2d shows the values for the (222)/(130) perovskite peak at 2θ = 31.9°, chosen because it has the highest signal-to-noise ratio across all films. The fwhm can again be seen to increase as the substrate temperature during growth increases, with the large grain film L having fwhm at the instrument response limit, while film H has again the highest fwhm, indicating the smallest crystallites.

To further probe the crystal quality of the different films, we also performed Urbach energy (E_U) measurements (Figure 2b) from the photocurrent onsets of the external quantum efficiency (EQE) spectra (Figure S10), which give a measure of electronic disorder. Our data shows that the large grain, low substrate temperature film L does indeed have the lowest E_U at 12.5 meV, increasing to 13.3 meV for the room temperature sample, indicating that the largest grains do correspond to the least energetic disorder. However, detailed analysis has shown that in the case where $E_U < kT = 26$ meV for $T = 298$ K (where k is the Boltzmann constant, and T is the temperature), the expected change in V_{OC} is small,[42] such that only minor improvements are expected from the E_U decrease in this case.

Together, the E_U and XRD measurements confirm that the large crystals seen in SEM directly reflect better crystal quality within the material, with a lower U_b and XRD fwhm that fall below the instrument response. The samples with the largest grains, L and HL, also do not show the presence of crystalline excess PbI_2, suggesting that a balanced stoichiometry could play a part in the growth of larger grains. All of these factors could be expected to be indicative of improved performance, and a more in depth study of the device operation is now needed to understand why this is not the case.

Figure 3a shows box plots of the $J-V$ characteristics measured from devices L, HL, LH, and HLH. As outlined previously, the large-grain devices L have lower J_{SC} and V_{OC} than those of the small grain devices H, resulting in a decrease in PCE from 16.0% (15.2% steady state) for the latter to 10.1% (9.4% steady state) for the former. The J_{SC} increases in spite of the perovskite film thickness decreasing for H. Indeed, when the small grain $MAPbI_3$ layer thickness was increased to a more optimal thickness of 600 nm, we produced a champion device of efficiency 18.2% (17.5% steady state) (Figure S9), showing

https://dx.doi.org/10.1021/acsenergylett.0c00183
ACS Energy Lett. 2020, 5, 710−717

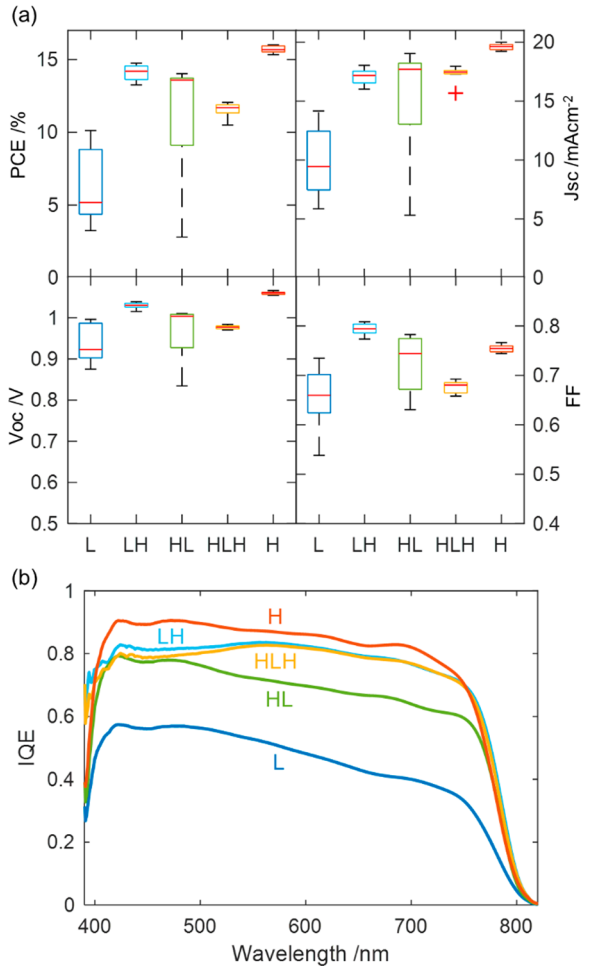

Figure 3. (a) Box plots of the *J*–*V* characteristics taken from eight devices made according to the five different deposition conditions. (b) Internal quantum efficiency (IQE) curves of the highest performing device measured from each of the five different deposition conditions.

that the difference in performance is even greater for comparable light absorption.

To better understand the origin of the difference in performance across the devices, we performed internal quantum efficiency (IQE) measurements (Figure 3b). IQE measures the probability that an electron–hole pair will be generated and collected as photocurrent by a photon of a specific wavelength absorbed in the device, and it is obtained by normalizing the EQE (Figure S10) with respect to the absorptance (Figure S11) of the devices. This corrects the EQE for losses due to photons reflected off or transmitted through the device and means IQE only drops as a result of losing photocurrent via charge trapping or recombination of photogenerated charge. For our devices, most notably L and HL, the loss in charge carriers collected is not uniform across the photon energy spectrum, but rather it drops off with increasing wavelength. Because the absorption coefficient of $MAPbI_3$ increases rapidly with photon energy above the band gap (Figure S12), in our devices, high-energy photons (short-wavelength light) will be absorbed and produce free-carriers with a sharp exponentially decaying density profile, peaked at the interface with C_{60}. In contrast, lower-energy photons (longer-wavelength light) will be absorbed more uniformly over the thickness of the $MAPbI_3$ layer. The slanted IQE curve hence indicates that there is a fundamental problem collecting charges generated deeper in the large grain device L.

Because the cells are oriented in such a way that the light passes through the C_{60}/perovskite interface first, these results point to a problem with the collection of electrons. Indeed, electrons are the charge-carriers that on average need to travel a shorter distance if light is absorbed near the interface, but comparatively further if light is absorbed deeper in the film. This could be due to either poorer electron mobility or lifetime in the larger grains preventing the electrons generated deeper in the film from reaching the ETL, or a result of poor interface optimization resulting in increased back surface recombination at the HTL leading to nonradiative recombination.

Our optical-pump THz-probe spectroscopy (OPTPS) measurements suggest that it is a combination of both effects. OPTPS revealed lower charge-carrier mobilities for films grown on low-temperature substrates (6.87 $cm^2/(V\ s)$) compared with those grown at room temperature (13.0 $cm^2/(V\ s)$), providing evidence that contrary to expectations, the intrinsic electrical properties are poorer for the large-crystal devices. On the other hand, analysis of the J_{sc} and integrated current from the EQE measurements, displayed in Figure S13, show improved current and EQE for the LH, HL, and HLH devices, where the perovskite material at the interface with the CTL has been grown at a different temperature than the bulk. This indicates that interface morphology also significantly affects device performance, with the most benefit obtained when growing the perovskite near the HTL at a higher temperature than that of the bulk. Strikingly, the comparatively worse performance of HLH shows that it is significantly better to only change the composition of the perovskite near one interface rather than both.

The simplest explanation for this phenomenon is that the larger grains present more traps for the electrons, limiting their diffusion lengths and hence collection. The partial recovery of the EQE when incorporating smaller grains at the perovskite-CTL interfaces indicates either that these traps are mainly located at these interfaces, or that the material grown on a small grain template is simply less prone to traps in the case of HL. This seemingly goes against the idea that traps are associated with grain boundaries, since the large grain samples necessarily have significantly fewer boundaries, so possibly the answer lies more in the stoichiometry of the boundary, as outlined by Jacobsson et al.[43] Indeed, in contrast to the other films, film L shows larger, darker regions between the grains, in both the cross section and top-down SEM images. These regions are probably a result of electron beam damage and hence a likely indicator of excess organic material, which is more vulnerable to this damage than the rest of the film.[44] Excess PbI_2 has previously been associated with higher-performance solution processed devices,[45] specifically being linked with trap passivation at the grain boundaries[46] or at the ETL interface, mesoporous TiO_2 in this case.[47] Notably, Jacobsson et al. associate the worse photovoltaic performance without a PbI_2 excess with excess organic molecules at grain boundaries.[43] We believe this to be the case here as well given our direct evidence from the XRD (Figure 2c) linking higher performance devices with excess PbI_2 and the increased susceptibility to electron beam damage of the grain boundaries in the films grown at low temperature (L) (Figure S2). This is in contrast to the work previously done by Xu et al. that showed improved performance when the PbI_2 layer at the n-type interface was removed, though this work was performed

https://dx.doi.org/10.1021/acsenergylett.0c00183
ACS Energy Lett. 2020, 5, 710–717

on devices with TiO_2 rather than C_{60} as the n-type contact, which could play a large role in the crystallization dynamics.[48] In vacuum co-evaporated devices, remnant PbI_2 has also been shown to contribute directly to photocurrent.[49] It is worth noting that excess unreacted PbI_2 has also been associated with photoinstability of the resulting films,[50] and previous reports agree that it is only beneficial up to a point.[45]

We now address the mechanism that determines crystal size in evaporated polycrystalline films of $MAPbI_3$. In particular, does substrates temperature simply affect crystal size by changing the film stoichiometry as a result of changed MAI adsorption, or does temperature also play a more direct role in crystallization? We found that both low temperature and a balanced stoichiometry are needed to grow large grains, as increasing the MAI flux with the substrate at room temperature did not result in large grains and left the performance of the devices relatively unchanged (Figure S17). In contrast, decreasing the MAI flux for low substrate temperature conditions did replicate the mixed phase seen in the H samples, though the performance was only matched if the initial interface was grown at room temperature (Figure S18). This is clear evidence that the benefits of excess PbI_2 for vacuum co-evaporation come not only in the form of direct passivation in the bulk or at grain boundaries, but that it also plays a crucial role in templating the growth of a material with better charge carrier properties. Indeed, HL shows no excess crystalline PbI_2 but still exhibits improved J_{sc} on par with the other samples that have at least one interface grown at room temperature (LH and HLH). Thus, it is likely that the presence of PbI_2 domains during the growth of the films leads to better growth conditions for photovoltaic performance, irrespective of whether the PbI_2 gets converted in the end.

We hypothesize that the beneficial effects of excess PbI_2 during $MAPbI_3$ growth via co-evaporation come from PbI_2 domains templating the growth of $MAPbI_3$. Indeed, we found that the presence of PbI_2 greatly enhances the adsorption of MAI, as when depositing MAI on its own we did not observe MAI sticking to either FTO or glass. This hypothesis is also consistent with our observation of a higher adsorption rate of MAI to a quartz microbalance thickness monitor in the vicinity of the substrate where PbI_2 is present, compared with one in the PbI_2-free region near the MAI crucible. Together, these results suggest that PbI_2 deposits first on the substrate, subsequently adsorbing MAI and converting to $MAPbI_3$. Lower substrate temperatures then directly increase the sticking coefficient of MAI onto PbI_2. As such, while previous reports had found growth to vary with stoichiometry,[24−26] we find that both a balanced stoichiometry and rapid perovskite conversion are needed to produce large grains. This also explains why increasing substrate temperature above 20 °C does not lead to the desired performance boost (Figure S19),[51] due to too much excess PbI_2 being present during film formation, even if it is entirely converted by the end of the deposition.[52]

Finally, to address the substrate rate control method used in this work more generally, we found it to be a direct and versatile way of reproducibly controlling MAI flux. Indeed, using substrate rate control, we found consistent and reproducible performance for devices co-deposited using MAI precursors from different suppliers, which had very different adsorption behavior on their own (Figure S20). Increasing the thickness for device optimization also proved as simple as running the evaporation for longer, and continuing to ramp up the MAI crucible temperature to keep the substrate rate constant. This method works well because, as discussed previously, MAI has significantly increased adsorption in the presence of PbI_2, as we found much higher rates measured near the substrate than the individual contributions of PbI_2 and MAI when heating them up alone. The champion device achieved via our substrate rate control deposition method is the 18.2% PCE device grown at room temperature (20 °C) presented earlier (Figure S9), and it shows the potential of this technique as a novel way of tuning MHP vacuum co-deposition.

In conclusion, our work demonstrates control of crystallite size in vacuum co-evaporated films of $MAPbI_3$ by tuning the temperature of the substrate during deposition. Films grown at low temperature (−2 °C) exhibited large, micrometer-sized grains but significantly reduced J_{SC}, dropping the performance from PCE = 16.0% to 10.1% as compared to films grown at room temperature (23 °C). We find changing the substrate temperature directly affects MAI adsorption rate, changing both the conversion rate of PbI_2 to $MAPbI_3$ as well as final stoichiometry. Grain growth and morphology is then a result of both of these parameters, which can be tuned individually by also changing the MAI sublimation rate at the MAI source. Furthermore, we find strong evidence to suggest that the deposition process happens through deposition of PbI_2 on the substrate first, followed by subsequent conversion to $MAPbI_3$, as opposed to a simultaneous process. The difference in performance of our devices indicates that excess PbI_2 is beneficial to device performance both during deposition by seeding growth and in the final film by passivating charge carrier traps at grain boundaries. To achieve optimal performance, both the amount of MAI vapor incident on the substrate and the conversion rate of PbI_2 to $MAPbI_3$ must be optimized, which can only be done through changing the substrate temperature. This work provides a significant advancement in understanding the growth mechanism of vacuum co-evaporated $MAPbI_3$ and offers a new avenue to optimize solar cells made from both this and more complex MHP formulations. With the ability to control grain size through substrate temperature, we expect further advancements will be made with subsequent passivation methodologies to obtain large crystalline domains with low defect densities and long carrier lifetimes, thereby leading to scalable, more efficient, and highly reproducible MHP solar cell devices.

■ ASSOCIATED CONTENT

Supporting Information

The Supporting Information is available free of charge at https://pubs.acs.org/doi/10.1021/acsenergylett.0c00183.

Additional details about device fabrication and experimental procedures, as well as additional SEM images, absorbance and absorptance spectra, IQE spectra, OPTPS spectra, steady-state PL spectra, TRPL spectra, and additional experiments such as annealing dependence of devices, changing MAI flux at fixed temperature, and comparing substrate rate for different MAI precursors (PDF)

https://dx.doi.org/10.1021/acsenergylett.0c00183
ACS Energy Lett. 2020, 5, 710−717

AUTHOR INFORMATION

Corresponding Author

Michael B. Johnston − *Department of Physics, University of Oxford, Oxford OX1 3PU, United Kingdom;* orcid.org/0000-0002-0301-8033; Email: Michael.johnston@physics.ox.ac.uk

Authors

Kilian B. Lohmann − *Department of Physics, University of Oxford, Oxford OX1 3PU, United Kingdom*

Jay B. Patel − *Department of Physics, University of Oxford, Oxford OX1 3PU, United Kingdom*

Mathias Uller Rothmann − *Department of Physics, University of Oxford, Oxford OX1 3PU, United Kingdom*

Chelsea Q. Xia − *Department of Physics, University of Oxford, Oxford OX1 3PU, United Kingdom*

Robert D. J. Oliver − *Department of Physics, University of Oxford, Oxford OX1 3PU, United Kingdom*

Laura M. Herz − *Department of Physics, University of Oxford, Oxford OX1 3PU, United Kingdom;* orcid.org/0000-0001-9621-334X

Henry J. Snaith − *Department of Physics, University of Oxford, Oxford OX1 3PU, United Kingdom;* orcid.org/0000-0001-8511-790X

Complete contact information is available at: https://pubs.acs.org/10.1021/acsenergylett.0c00183

Notes

The authors declare the following competing financial interest(s): H.J.S. is the cofounder and CSO of Oxford PV Ltd, a company that is commercializing perovskite photovoltaic technologies.

ACKNOWLEDGMENTS

The authors would like to thank the Engineering and Physical Sciences Research Council (UK) (EPSRC) for financial support. M.B.J. thanks the Humboldt Foundation. R.D.J.O. gratefully acknowledges funding via a Penrose Scholarship.

REFERENCES

(1) Kojima, A.; Teshima, K.; Shirai, Y.; Miyasaka, T. Organometal Halide Perovskites as Visible-Light Sensitizers for Photovoltaic Cells. *J. Am. Chem. Soc.* **2009**, *131*, 6050.

(2) Stranks, S. D.; Snaith, H. J. Metal-halide perovskites for photovoltaic and light-emitting devices. *Nat. Nanotechnol.* **2015**, *10*, 391.

(3) NREL. Best Research-Cell Efficiency Chart; U.S. Department of Energy; https://www.nrel.gov/pv/cell-efficiency.html.

(4) Noh, J. H.; Im, S. H.; Heo, J. H.; Mandal, T. N.; Seok, S. I. Chemical Management for Colorful, Efficient, and Stable Inorganic−Organic Hybrid Nanostructured Solar Cells. *Nano Lett.* **2013**, *13*, 1764.

(5) McMeekin, D. P.; Sadoughi, G.; Rehman, W.; Eperon, G. E.; Saliba, M.; Hörantner, M. T.; Haghighirad, A.; Sakai, N.; Korte, L.; Rech, B.; Johnston, M. B.; Herz, L. M.; Snaith, H. J. A mixed-cation lead mixed-halide perovskite absorber for tandem solar cells. *Science* **2016**, *351*, 151.

(6) Stoumpos, C. C.; Malliakas, C. D.; Kanatzidis, M. G. Semiconducting Tin and Lead Iodide Perovskites with Organic Cations: Phase Transitions, High Mobilities, and Near-Infrared Photoluminescent Properties. *Inorg. Chem.* **2013**, *52*, 9019.

(7) Li, Z.; Yang, M.; Park, J.-S.; Wei, S.-H.; Berry, J. J.; Zhu, K. Stabilizing Perovskite Structures by Tuning Tolerance Factor: Formation of Formamidinium and Cesium Lead Iodide Solid-State Alloys. *Chem. Mater.* **2016**, *28*, 284.

(8) Levchuk, I.; Osvet, A.; Tang, X.; Brandl, M.; Perea, J. D.; Hoegl, F.; Matt, G. J.; Hock, R.; Batentschuk, M.; Brabec, C. J. Brightly Luminescent and Color-Tunable Formamidinium Lead Halide Perovskite FAPbX3 (X = Cl, Br, I) Colloidal Nanocrystals. *Nano Lett.* **2017**, *17*, 2765.

(9) Eperon, G. E.; Leijtens, T.; Bush, K. A.; Prasanna, R.; Green, T.; Wang, J. T.-W.; McMeekin, D. P.; Volonakis, G.; Milot, R. L.; May, R.; Palmstrom, A.; Slotcavage, D. J.; Belisle, R. A.; Patel, J. B.; QXX.; et al. Perovskite-perovskite tandem photovoltaics with optimized bandgaps. *Science* **2016**, *354*, 861.

(10) Yang, Z.; Rajagopal, A.; Chueh, C.-C.; Jo, S. B.; Liu, B.; Zhao, T.; Jen, A. K.-Y. Stable Low-Bandgap Pb−Sn Binary Perovskites for Tandem Solar Cells. *Adv. Mater.* **2016**, *28*, 8990.

(11) Anaya, M.; Lozano, G.; Calvo, M. E.; Míguez, H. ABX3 Perovskites for Tandem Solar Cells. *Joule* **2017**, *1*, 769.

(12) Oxford PV perovskite solar cell achieves 28% efficiency. Oxford PV, 2018; https://www.oxfordpv.com/news/oxford-pv-perovskite-solar-cell-achieves-28-efficiency.

(13) Ávila, J.; Momblona, C.; Boix, P. P.; Sessolo, M.; Bolink, H. J. Vapor-Deposited Perovskites: The Route to High-Performance Solar Cell Production? *Joule* **2017**, *1*, 431.

(14) Forgács, D.; Gil-Escrig, L.; Pérez-Del-Rey, D.; Momblona, C.; Werner, J.; Niesen, B.; Ballif, C.; Sessolo, M.; Bolink, H. J. Efficient Monolithic Perovskite/Perovskite Tandem Solar Cells. *Adv. Mater.* **2017**, *7*, 1602121.

(15) Momblona, C.; Gil-Escrig, L.; Bandiello, E.; Hutter, E. M.; Sessolo, M.; Lederer, K.; Blochwitz-Nimoth, J.; Bolink, H. J. Efficient vacuum deposited p-i-n and n-i-p perovskite solar cells employing doped charge transport layers. *Energy Environ. Sci.* **2016**, *9*, 3456.

(16) Borchert, J.; Milot, R. L.; Patel, J. B.; Davies, C. L.; Wright, A. D.; Maestro, L. M.; Snaith, H. J.; Herz, L. M.; Johnston, M. B. Large-Area, Highly Uniform Evaporated Formamidinium Lead Triiodide Thin Films for Solar Cells. *ACS Energy Lett.* **2017**, *2*, 2799.

(17) Longo, G.; Momblona, C.; La-Placa, M.-G.; Gil-Escrig, L.; Sessolo, M.; Bolink, H. J. Fully Vacuum-Processed Wide Band Gap Mixed-Halide Perovskite Solar Cells. *ACS Energy Lett.* **2018**, *3*, 214.

(18) Gil-Escrig, L.; Momblona, C.; La-Placa, M.-G.; Boix, P. P.; Sessolo, M.; Bolink, H. J. "Vacuum Deposited Triple-Cation Mixed-Halide Perovskite Solar Cells. *Adv. Energy Mater.* **2018**, *8*, 1703506.

(19) Ball, J. M.; Buizza, L.; Sansom, H. C.; Farrar, M. D.; Klug, M. T.; Borchert, J.; Patel, J.; Herz, L. M.; Johnston, M. B.; Snaith, H. J. Dual-Source Coevaporation of Low-Bandgap FA1−xCsxSn1−yPbyI3 Perovskites for Photovoltaics. *ACS Energy Lett.* **2019**, *4*, 2748.

(20) Borchert, J.; Levchuk, I.; Snoek, L. C.; Rothmann, M. U.; Haver, R.; Snaith, H. J.; Brabec, C. J.; Herz, L. M.; Johnston, M. B. Impurity Tracking Enables Enhanced Control and Reproducibility of Hybrid Perovskite Vapour Deposition. *ACS Appl. Mater. Interfaces* **2019**, *11*, 28851.

(21) Liu, M.; Johnston, M. B.; Snaith, H. J. Efficient planar heterojunction perovskite solar cells by vapour deposition. *Nature* **2013**, *501*, 395.

(22) Patel, J. B.; Wong-Leung, J.; Van Reenen, S.; Sakai, N.; Wang, J. T. W.; Parrott, E. S.; Liu, M.; Snaith, H. J.; Herz, L. M.; Johnston, M. B. Influence of Interface Morphology on Hysteresis in Vapor-Deposited Perovskite Solar Cells. *Adv. Electron. Mater.* **2017**, *3*, 1600470.

(23) Tavakoli, M. M.; Simchi, A.; Mo, X.; Fan, Z. High-quality organohalide lead perovskite films fabricated by layer-by-layer alternating vacuum deposition for high efficiency photovoltaics. *Mater. Chem. Front.* **2017**, *1*, 1520.

(24) Hsiao, S.-Y.; Lin, H.-L.; Lee, W.-H.; Tsai, W.-L.; Chiang, K.-M.; Liao, W.-Y.; Ren-Wu, C.-Z.; Chen, C.-Y.; Lin, H.-W. Efficient All-Vacuum Deposited Perovskite Solar Cells by Controlling Reagent Partial Pressure in High Vacuum. *Adv. Mater.* **2016**, *28*, 7013.

(25) Teuscher, D. J.; Ulianov, D. A.; Müntener, P. O.; Grätzel, P. M.; Tétreault, D. N. Control and Study of the Stoichiometry in Evaporated Perovskite Solar Cells. *ChemSusChem* **2015**, *8*, 3847.

(26) Arivazhagan, V.; Xie, J.; Yang, Z.; Hang, P.; Parvathi, M. M.; Xiao, K.; Cui, C.; Yang, D.; Yu, X. Vacuum co-deposited

CH3NH3PbI3 films by controlling vapor pressure for efficient planar perovskite solar cells. *Sol. Energy* **2019**, *181*, 339.
(27) Kim, H. D.; Ohkita, H.; Benten, H.; Ito, S. Photovoltaic Performance of Perovskite Solar Cells with Different Grain Sizes. *Adv. Mater.* **2016**, *28*, 917.
(28) Nie, W.; Tsai, H.; Asadpour, R.; Blancon, J.-C.; Neukirch, A. J.; Gupta, G.; Crochet, J. J.; Chhowalla, M.; Tretiak, S.; Alam, M. A.; Wang, H.-L.; Mohite, A. D. High-efficiency solution-processed perovskite solar cells with millimeter-scale grains. *Science* **2015**, *347*, 522.
(29) Chiang, C.; Wu, C. Film Grain-Size Related Long-Term Stability of Inverted Perovskite Solar Cells. *ChemSusChem* **2016**, *9*, 2666.
(30) Han, Q.; Bai, Y.; Liu, J.; Du, K.-z.; Li, T.; Ji, D.; Zhou, Y.; Cao, C.; Shin, D.; Ding, J.; Franklin, A. D.; Glass, J. T.; Hu, J.; Therien, M. J.; Liu, J.; Mitzi, D. B. Additive engineering for high-performance room-temperature-processed perovskite absorbers with micron-size grains and microsecond-range carrier lifetimes. *Energy Environ. Sci.* **2017**, *10*, 2365.
(31) Yin, W.-J.; Shi, T.; Yan, Y. Unique Properties of Halide Perovskites as Possible Origins of the Superior Solar Cell Performance. *Adv. Mater.* **2014**, *26*, 4653.
(32) Yun, J. S.; Ho-Baillie, A.; Huang, S.; Woo, S. H.; Heo, Y.; Seidel, J.; Huang, F.; Cheng, Y.-B.; Green, M. A. Benefit of Grain Boundaries in Organic−Inorganic Halide Planar Perovskite Solar Cells. *J. Phys. Chem. Lett.* **2015**, *6*, 875.
(33) Yun, J. S.; Seidel, J.; Kim, J.; Soufiani, A. M.; Huang, S.; Lau, J.; Jeon, N. J.; Seok, S. I.; Green, M. A.; Ho-Baillie, A. Critical Role of Grain Boundaries for Ion Migration in Formamidinium and Methylammonium Lead Halide Perovskite Solar Cells. *Adv. Energy Mater.* **2016**, *6*, 1600330.
(34) Adhyaksa, G. W. P.; Brittman, S.; Āboliņš, H.; Lof, A.; Li, X.; Keelor, J. D.; Luo, Y.; Duevski, T.; Heeren, R. M. A.; Ellis, S. R.; Fenning, D. P.; Garnett, E. C. Understanding Detrimental and Beneficial Grain Boundary Effects in Halide Perovskites. *Adv. Mater.* **2018**, *30*, 1804792.
(35) Crothers, T. W.; Milot, R. L.; Patel, J. B.; Parrott, E. S.; Schlipf, J.; Müller-Buschbaum, P.; Johnston, M. B.; Herz, L. M. Photon Reabsorption Masks Intrinsic Bimolecular Charge-Carrier Recombination in CH3NH3PbI3 Perovskite. *Nano Lett.* **2017**, *17*, 5782.
(36) Nie, W.; Tsai, H.; Blancon, J.; Liu, F.; Stoumpos, C. C.; Traore, B.; Kepenekian, M.; Durand, O.; Katan, C.; Tretiak, S.; Crochet, J.; Ajayan, P. M.; Kanatzidis, M. G.; Even, J.; Mohite, A. D. Critical Role of Interface and Crystallinity on the Performance and Photostability of Perovskite Solar Cell on Nickel Oxide. *Adv. Mater.* **2018**, *30*, 1703879.
(37) Chen, J.; Zuo, L.; Zhang, Y.; Lian, X.; Fu, W.; Yan, J.; Li, J.; Wu, G.; Li, C.; Chen, H. High-Performance Thickness Insensitive Perovskite Solar Cells with Enhanced Moisture Stability. *Adv. Energy Mater.* **2018**, *8*, 1800438.
(38) Song, S.; Hörantner, M. T.; Choi, K.; Snaith, H. J.; Park, T. Inducing swift nucleation morphology control for efficient planar perovskite solar cells by hot-air quenching. *J. Mater. Chem. A* **2017**, *5*, 3812.
(39) Ren, Y.-K.; Ding, X.-H.; Wu, Y.-H.; Zhu, J.; Hayat, T.; Alsaedi, A.; Xu, Y.-F.; Li, Z.-Q.; Yang, S.-F.; Dai, S.-Y. Temperature-assisted rapid nucleation: a facile method to optimize the film morphology for perovskite solar cells. *J. Mater. Chem. A* **2017**, *5*, 20327.
(40) Bækbo, M. J.; Hansen, O.; Chorkendorff, I.; Vesborg, P. C. K. Deposition of methylammonium iodide via evaporation − combined kinetic and mass spectrometric study. *RSC Adv.* **2018**, *8*, 29899.
(41) Scherrer, P. Bestimmung der Größe und der inneren Struktur von Kolloidteilchen mittels Röntgenstrahlen. *Göttinger Nachrichten Math. Phys.* **1918**, *2*, 98.
(42) Nayak, P. K.; Mahesh, S.; Snaith, H. J.; Cahen, D. Photovoltaic solar cell technologies: analysing the state of the art. *Nature Reviews Materials* **2019**, *4*, 269.
(43) Jacobsson, T. J.; Correa-Baena, J.-P.; Anaraki, E. H.; Philippe, B.; Stranks, S. D.; Bouduban, M. E. F.; Tress, W.; Schenk, K.; Teuscher, J.; Moser, J.-E.; Rensmo, H.; Hagfeldt, A. Unreacted PbI2 as a Double-Edged Sword for Enhancing the Performance of Perovskite Solar Cells. *J. Am. Chem. Soc.* **2016**, *138*, 10331.
(44) Rothmann, M. U.; Li, W.; Zhu, Y.; Liu, A.; Ku, Z.; Bach, U.; Etheridge, J.; Cheng, Y.-B. Structural and Chemical Changes to CH3NH3PbI3 Induced by Electron and Gallium Ion Beams. *Adv. Mater.* **2018**, *30*, 1800629.
(45) Kim, Y. C.; Jeon, N. J.; Noh, J. H.; Yang, W. S.; Seo, J.; Yun, J. S.; Ho-Baillie, A.; Huang, S.; Green, M. A.; Seidel, J.; Ahn, T. K.; Seok, S. I. Beneficial Effects of PbI2 Incorporated in Organo-Lead Halide Perovskite Solar Cells. *Adv. Energy Mater.* **2016**, *6*, 1502104.
(46) Wang, L.; McCleese, C.; Kovalsky, A.; Zhao, Y.; Burda, C. Femtosecond Time-Resolved Transient Absorption Spectroscopy of CH3NH3PbI3 Perovskite Films: Evidence for Passivation Effect of PbI2. *J. Am. Chem. Soc.* **2014**, *136*, 12205.
(47) Cao, D. H.; Stoumpos, C. C.; Malliakas, C. D.; Katz, M. J.; Farha, O. K.; Hupp, J. T.; Kanatzidis, M. G. Remnant PbI2, an unforeseen necessity in high-efficiency hybrid perovskite-based solar cells? *APL Mater.* **2014**, *2*, No. 091101.
(48) Xu, H.; Xu, F.; Wang, W.; Zhu, Y.; Fang, Z.; Yao, B.; Hong, F.; Cui, J.; Xu, F.; Xu, R.; Chen, C.-C.; Wang, L. Resolving the detrimental interface in co-evaporated MAPbI3 perovskite solar cells by hybrid growth method. *Org. Electron.* **2019**, *69*, 329.
(49) Patel, J. B.; Lin, Q.; Zadvorna, O.; Davies, C. L.; Herz, L. M.; Johnston, M. B. Photocurrent Spectroscopy of Perovskite Solar Cells Over a Wide Temperature Range from 15 to 350 K. *J. Phys. Chem. Lett.* **2018**, *9*, 263.
(50) Liu, F.; Dong, Q.; Wong, M. K.; Djurišić, A. B.; Ng, A.; Ren, Z.; Shen, Q.; Surya, C.; Chan, W. K.; Wang, J.; Ng, A. M. C.; Liao, C.; Li, H.; Shih, K.; Wei, C.; Su, H.; Dai, J. Is Excess PbI2 Beneficial for Perovskite Solar Cell Performance? *Adv. Energy Mater.* **2016**, *6*, 1502206.
(51) Wang, S.; Ono, L. K.; Leyden, M. R.; Kato, Y.; Raga, S. R.; Lee, M. V.; Qi, Y. Smooth perovskite thin films and efficient perovskite solar cells prepared by the hybrid deposition method. *J. Mater. Chem. A* **2015**, *3*, 14631.
(52) Kottokkaran, R.; Gaonkar, H. A.; Abbas, H. A.; Noack, M.; Dalal, V. Performance and stability of co-evaporated vapor deposited perovskite solar cells. *J. Mater. Sci.: Mater. Electron.* **2019**, *30*, 5487.

https://dx.doi.org/10.1021/acsenergylett.0c00183
ACS Energy Lett. 2020, 5, 710−717